Applied Catalysis B: Environmental 236 (2018) 205–211

Contents lists available at ScienceDirect

Applied Catalysis B: Environmental

journal homepage: www.elsevier.com/locate/apcatb

Constructing a novel $Bi_2SiO_5/BiPO_4$ heterostructure with extended light response range and enhanced photocatalytic performance

Di Liu[a], Weibin Cai[a], Yonggang Wang[a,*], Yongfa Zhu[b,*]

[a] School of Chemical & Environmental Engineering, China University of Mining & Technology, Beijing, 100083, PR China
[b] Department of Chemistry, Tsinghua University, Beijing, 100084, PR China

ARTICLE INFO

Keywords:
$BiPO_4$
Bi_2SiO_5
Heterostructure
Photocatalysis

ABSTRACT

To further extend the light response range of $BiPO_4$ and meanwhile keep its strong photocatalytic oxidation ability, the design of a type-II heterojunction by coupling $BiPO_4$ with a narrower band gap semiconductor of Bi_2SiO_5 as a novel and efficient photocatalytic catalyst has been successfully realized through a simple co-precipitate method. Moreover, under 365 nm UV light irradiation, pure $BiPO_4$ shows no photo-activity, whereas the optimal $Bi_2SiO_5/BiPO_4$ heterostructure exhibits highly enhanced photocatalytic activity than pure Bi_2SiO_5 in systems of photo-degradation over phenol and MB, which is 4.36 times and 1.13 times the values of pure Bi_2SiO_5. Experimental results reveal that the superior photocatalytic performance can be attributed to the synergetic effect of the evidently improved charge separation ability via the heterojunction, good crystallinity, expanded light absorbance and the moderate BET specific surface area.

1. Introduction

Recently, Bi-based nonmetal oxysalts, including $Bi_2O_2CO_3$, $BiPO_4$ and Bi_2SiO_5, have attracted great attention due to their characteristic photocatalytic activities originating from their high crystallinity and surface modification effect of the nonmetal oxyacid root [1,2]. Recently, Zhu's group [3] successfully synthesized a new photocatalyst of $BiPO_4$ with excellent photo-stability and a higher photocatalytic efficiency compared to TiO_2 (Degussa P25), though its BET surface area was only 1/10 of P25. Nevertheless, $BiPO_4$ still falls far short of what the ideal photocatalyst required due to its wide bandgap and low electron–hole separation efficiency [4]. Design and fabrication of $BiPO_4$-based heterojunction structure has proven to be an effective strategy. Much progress has been achieved for $BiPO_4$ through constructing heterostructured photocatalysts with other narrow-band-gap semiconductors, including $Ag_3PO_4/BiPO_4$ [5], $AgBr/BiPO_4$ [6,7], $AgI/BiPO_4$ [8], $BiOCl/BiPO_4$ [9], $BiOBr/BiPO_4$ [10–13], $BiOI/BiPO_4$ [14], $Bi_2O_2CO_3/BiPO_4$ [15], $g\text{-}C_3N_4/BiPO_4$ [16–18], $BiVO_4/BiPO_4$ [19], $Cu_2O/Au/BiPO_4$ [20] and so on. In spite of this, it is still essential to filter suitable hetero-junction component for $BiPO_4$ that can effectively expand the light response range of the system and remain its strong photocatalytic oxidation ability.

As a member of Bi-based nonmetal oxysalts, Bi_2SiO_5 was also reported to be an effective photocatalytic material in the removal of water pollutant [21], and it possesses a narrower band-gap of 3.54 eV than $BiPO_4$ [22]. What's more, as previously reported, the conduction band of $BiPO_4$ ($E_{CB} = -0.65$ eV) is more negative than that of Bi_2SiO_5 ($E_{CB} = 0.05$ eV), while the valence band of $BiPO_4$ ($E_{VB} = 3.2$ eV) is more shallower than that of Bi_2SiO_5 ($E_{VB} = 3.59$ eV) [3,22]. Therefore, the two components of $BiPO_4$ and Bi_2SiO_5 possess matched band potentials which can promote the flow of charge carriers via the heterojunction interfaces [23], the design of a type-II heterojunction by coupling $BiPO_4$ with a narrower band gap semiconductor of Bi_2SiO_5 as a novel and powerful photocatalytic catalyst system is reasonable. As expected, our study successfully construct the novel heterostructure of $Bi_2SiO_5/BiPO_4$ through a simple co-precipitation hydrothermal method. The introduction of the component Bi_2SiO_5 has successfully broadened the spectral response range of the heterostructured system, and the optimal $Bi_2SiO_5/BiPO_4$ heterostructure shows highly improved photocatalytic activity than pure $BiPO_4$ and Bi_2SiO_5 in photo-degradation on phenol and MB.

2. Experimental

2.1. Materials preparation

Preparation of the heterostructured samples: In a typical reaction, 6 mmol $Bi(NO_3)_3{\cdot}5H_2O$, 2 mmol $NaH_2PO_4{\cdot}2H_2O$, Na_2SiO_3 (1 mmol, 2 mmol, 4 mmol, 6 mmol) was dissolved together in a beaker with 30 mL distilled water, and the solutions were stirred at room

* Corresponding authors.
E-mail addresses: wyg1960@126.com (Y. Wang), zhuyf@tsinghua.edu.cn (Y. Zhu).

https://doi.org/10.1016/j.apcatb.2018.05.022
Received 12 March 2018; Received in revised form 2 May 2018; Accepted 7 May 2018
Available online 08 May 2018

temperature for 5 min. The pH values of the above solutions were then adjusted to 1 with a HNO_3 solution (1 M) under vigorous stirring. After being stirred for another 30 min, the resulting precursor solutions were transferred into a 40 mL capacity Teflon-lined autoclave and hydrothermally treated at 160 ℃ for 24 h. When the reactions was finished, the autoclave was cooled to room temperature naturally. Eventually, the as-prepared precipitates were collected via centrifugation, washed with deionized water and ethanol for several times, and subsequently dried at 80 ℃ for 12 h. Products with different adding amount of Na_2SiO_3 ranging from 1 to 6 mmol were consequently denoted as S-1, S-2, S-4, S-6, respectively.

Sythesis of control samples (pure $BiPO_4$ and pure Bi_2SiO_5): Pure $BiPO_4$ was synthesized through a hydrothermal method previously reported [24]. Deionized water (80 mL), $NaH_2PO_4{\cdot}2H_2O$ (7.2 mmol) and $Bi(NO_3)_3{\cdot}5H_2O$ (2 mmol) were placed into a 100 mL beaker and stirred vigorously. The resulting precursor suspension was then hydrothermally treated at 160 ℃ for 24 h in a Teflon-lined autoclave of 100 mL capacity. After the reaction, the autoclave was cooled to room temperature naturally. The precipitates were collected by centrifugation, and washed with deionized water and ethanol for several times, and finally dried in oven at 120 ℃ for 10 h. For the synthesis of pure Bi_2SiO_5 [25], 6 mmol $Bi(NO_3)_3{\cdot}5H_2O$ and 3 mmol $Na_2SiO_3{\cdot}9H_2O$ was dissolved into 40 mL ethylene glycol and 40 mL deionized water under vigorous stirring, respectively. The $Na_2SiO_3{\cdot}9H_2O$ solution was then added to the solution of $Bi(NO_3)_3{\cdot}5H_2O$, a white suspension formed immediately. Finally, the pH of the mixed suspension was adjusted to 12 using a NaOH solution (2 M). After stirred for 30 min, the mixture was transferred into a Teflon-lined autoclave of 100 mL capacity and heated at 200 ℃ for 10 h. After the reaction, the autoclave was cooled to room temperature naturally. The precipitates were collected by centrifugation, and washed with deionized water and ethanol for several times, and finally dried in oven at 80 ℃ for 12 h.

2.2. Characterizations

A Rigaku D/max-2400 X-ray diff ;ractometer using a Cu Kα1 (λ = 0.15418 nm) at 40 kV and 200 mA was used to gain X-ray diffraction (XRD) patterns of the as-prepared samples. Fourier transform infrared spectra (FT-IR) were taken with a Bruker VERTEX 700 spectrometer in the frequency range of 1800–600 cm^{-1} with a resolution of 4 cm^{-1}. The morphologies and sizes of the as-prepared samples were collected at a SU-8010 field emission Scanning Electron Microscope (SEM). High-resolution transmission electron microscopy (HRTEM) images and energy dispersive spectrometer (EDS) analysis were obtained by a JEOL JEM-2010 F field emission transmission electron microscope with an accelerating voltage of 200 kV. The Brunauer–Emmett–Teller (BET) surface area measurements were performed using a Micromeritics (ASAP 2010 V5.02 H) surface area analyzer. The nitrogen adsorption and desorption isotherms were measured at 77 K after degassing the samples on a Sorptomatic 1900 Carlo Erba Instrument. UV–vis spectra and UV–vis diffuse reflectance spectra (DRS) were characterized with the aid of a Hitachi U-3010 UV–vis spectrophotometer. Electron spin resonance (ESR) spectra were recorded from the sample mixture, containing spin-trapping probes such as 5,5-dimethyl-1-pirroline-*N*-oxide (DMPO) and samples, after exposure to UV light for selected times using an Endor spectrometer (JEOL ES-ED3X) at room temperature. A standard three-electrode cell with ITO/photocatalyst sample as a working electrode, a platinum wire as a counter electrode, and a standard calomel electrode (SCE) as reference electrode were used in the photocurrent characterizations (UV light source was obtained by a xenon lamp with bandpass filter (350 ± 10 nm), among which 0.1 M Na_2SO_4 was used as the electrolyte solution (CHI-660E, China). The photocurrent responses of the photocatalysts upon light on and off were measured at 0.0 V. The electrochemical impedance spectroscopy (EIS) spectra of the photocatalysts upon light on and off were measured at 0.0 V with amplitude of sinusoidal wave at 10 mV and frequency range from 100 kHz to 0.01 Hz.

2.3. Photocatalytic experiments

Photo-degradation on two targeted pollutants of phenol and methylene blue (MB) under UV light (365 nm) irradiation was carried out to evaluate the photocatalytic activity of the as-prepared samples. The initial concentrations of phenol and MB are set as 10 ppm and 2×10^{-5} M, respectively. Before the light irradiation, a suspension of a 50 ml probe pollutants solution and 30 mg photocatalysts was stirred for 0.5 h under dark to reach the adsorption-desorption equilibrium. The UV light source was acquired by a 500 W xenon lamp equipped with a bandpass filter (365 ± 10 nm). At given time intervals, a suspension (2 mL) was extracted and centrifuged to remove the photocatalysts. The concentrations of probe pollutants were characterized by a HPLC system (Shimadzu LC-20AT) with a C18 reversed phase column and a Hitachi U-3010 UV–vis spectrophotometer.

3. Results and discussion

3.1. Formation of the heterostructure

The phase formation of the as-prepared samples synthesized through the co-precipitation method was investigated by XRD analysis. As shown in Fig. 1a, all samples exhibit similar XRD patterns with only

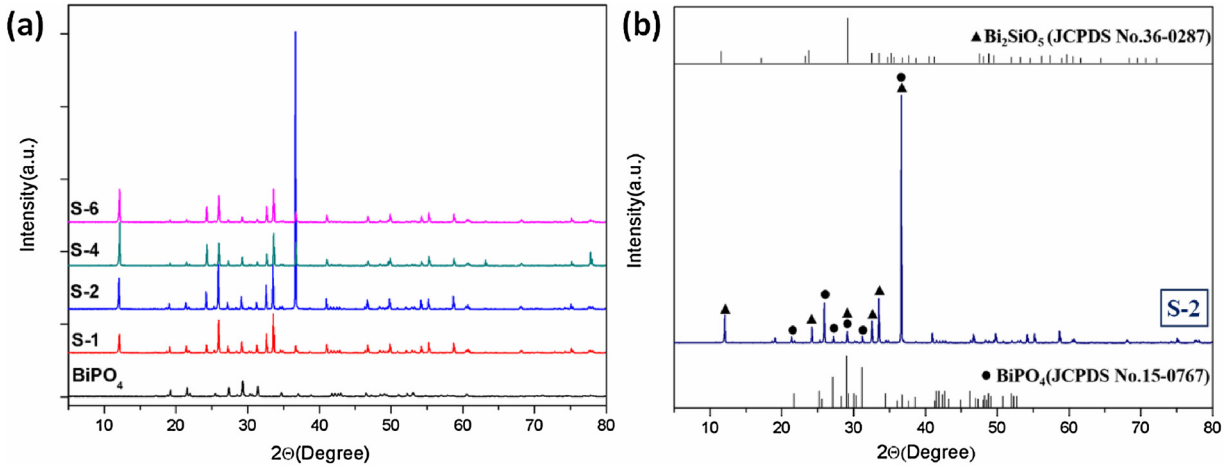

Fig. 1. XRD patterns of the as-prepared samples (a) and sample S-2 (b).

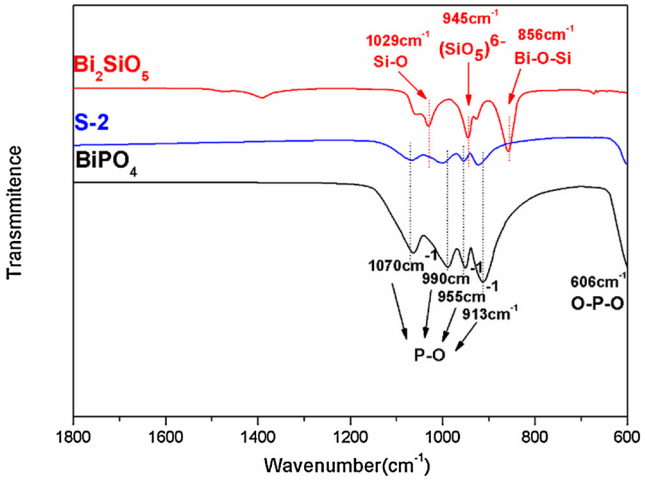

Fig. 2. FT-IR spectra of pure $BiPO_4$, pure Bi_2SiO_5 and sample S-2.

differences in the intensity of XRD peaks which may indicate different crystallinity and oriented growth of the grains during the hydrothermal reaction. It is well known that bulk defects would act as charge carrier traps for the recombination of photo-generated e^--h+ during the photocatalytic process. Good crystallinity indicates less bulk defects, and is supposed to be beneficial for photocatalysis. Among the as-prepared samples from S-1 to S-6, S-2 shows shark diffraction peaks with the highest intensity, indicating its good crystallinity. Additionally, from view of Fig. 1b, the diffraction peaks of S-2 can be indexed to the monoclinic phase of $BiPO_4$ (JCPDS 15–0767) and orthorhombic phase of Bi_2SiO_5 (JCPDS 36–0287). As a result, the co-existence peaks of Bi_2SiO_5 and $BiPO_4$ suggested that Bi_2SiO_5 and $BiPO_4$ successfully coupled together.

Fig. 2 shows the FT-IR spectra for pure $BiPO_4$, pure Bi_2SiO_5 and sample S-2. For pure $BiPO_4$, the υ_3 asymmetric stretching vibration of -PO_4 group splits into four absorption bands at 1071, 1002, 955 and 924 cm^{-1} [26]. For pure Bi_2SiO_5, the peaks located around 1029, 945 and 856 cm^{-1} correspond to the stretching vibration absorption of the Si—O bond, the isolated $(SiO_5)^{6-}$ groups and the Bi—O—Si bonds, respectively [27]. As for sample S-2, four broad absorption bands observed at the region of 900–1100 cm^{-1} can be attributed to the overlapping absorption peaks of υ_3 asymmetric bending modes of the -PO_4 units and the stretching vibration absorptions of Si-O bond, $(SiO_5)^{6-}$ groups. Therefore, combined with the above XRD result, FT-IR result would further ascertain the co-existence of Bi_2SiO_5 and $BiPO_4$ in sample S-2.

Obviously differentiable characteristics in the morphology of Bi_2SiO_5 and $BiPO_4$ can be found according to TEM, SEM and elemental mapping analysis as shown in Figs. 3 and 4 and S1. The distribution of elements in the components can be demonstrated by the technique of EDS mapping [28]. Hereby, EDS analysis (Fig. 3) shows peaks attributable to Bi, O, Si, P which is also indicative of the Bi_2SiO_5 component and $BiPO_4$ component exist in the as-prepared sample S-2. The TEM picture insert in Fig. 3 reveals two structures of rods and irregular plates. In the elemental mapping analysis, as the common element, Bi was found to be homogeneously distributed on the entire composite, however, it is noteworthy that the P element is exactly dispersed over the rod-like shape, while the Si element is found to be uniformly dispersed along the shape of irregular plates. This result indicates that the morphology of rods and irregular plates correspond to $BiPO_4$ and Bi_2SiO_5, respectively. Fig. S1 depicts the SEM micrographs of the as-prepared $Bi_2SiO_5/BiPO_4$ heterostructures with various SiO_3^{2-} adding amount at a low magnification. It can be seen that four samples exhibit similar morphologies and sizes, and plate-like Bi_2SiO_5 and rod-like $BiPO_4$ appeared in all the four as-prepared $Bi_2SiO_5/BiPO_4$ heterostructures. However, from view of the SEM pictures with higher magnification shown in Fig. 4, it is worth noting that sample S-2 has a larger number of well-defined rod-like structure with a larger ratio of length to diameter compared to other three samples, which may just account for its oriented growth along the axis of micro-rods and higher degree of crystallinity in comparison with other three $Bi_2SiO_5/BiPO_4$ heterostructures. Meanwhile, SEM picture of sample S-2 in Fig. 4 also reveals close attachment of $BiPO_4$ micro-rods to the surface of the Bi_2SiO_5 plates.

Further confirmation of the successful heterojunction structure of S-2 between Bi_2SiO_5 and $BiPO_4$ can be revealed by HRTEM analysis. As can be seen in Fig. 5, a clear interplanar spacing of 0.347 nm correspond to the (020) plane of $BiPO_4$, and the lattice spacing of 0.254 nm can be indexed to the d-spacing between (600) planes of Bi_2SiO_5, well confirming the formation of $Bi_2SiO_5/BiPO_4$ heterojunction and intimate connection between Bi_2SiO_5 and $BiPO_4$. Coupling with a narrower band gap component of Bi_2SiO_5, $BiPO_4$ can be supposed to obtain extended optical absorption. Moreover, the separation of photo-induced electron–hole pairs through the interfaces of $Bi_2SiO_5/BiPO_4$ heterojunction could be improved, as detailed in the following discussion.

3.2. Photocatalytic performance

The photocatalytic properties of as-prepared samples were evaluated under UV light irradiation (365 nm) by photo-degradation on two targeted pollutants, one is colorless phenol and the other is a common model methylene blue (MB). The rate constant k values of phenol and MB photo-degradation process were calculated from the fitted curves in Fig. 6 and are shown in Fig. S2a, b. No activity can be detected for pure $BiPO_4$ due to its wide band-gap revealed by the UV–vis diffuse reflection spectrum in Fig. 8a. All the as-prepared samples appear noticeable photo-activities in degradation of the two pollutants under the 365 nm light irradiation, indicating successfully extended optical absorption for these $Bi_2SiO_5/BiPO_4$ heterostructures. And along with the increase of SiO_3^{2-}, it is found that the photocatalytic performances of the as-prepared samples both first increase and then decrease in photo-degradation of the two targeted pollutants from observation of Fig. 6. The $Bi_2SiO_5/BiPO_4$ heterostructure of S-2 displayed the best photocatalytic activity among them. In addition, S-2 also shows higher photocatalytic activity than pure Bi_2SiO_5 with k value of 0.00946 min^{-1} for phenol system and 0.00953 for MB system, which is 4.36 times and 1.13 times the values of pure Bi_2SiO_5, respectively. In situ active species during the photocatalytic reaction can be detected through ESR technique. As can be seen in Fig. 7, by using DMPO as spin probe[29], existence of $O_2^{\cdot -}$ and ·OH were proved through the appearance of $O_2^{\cdot -}$ and ·OH signals upon UV light irradiation, moreover, the peaks intensity increased with prolonging the irradiation time. In addtion, the cyclic degradation experiments over the catalyst was also conducted to test its stability. As displayed in Fig. S2c, the experimental result of three continuous cyclic photo-degradation on phenol revealed a decent stability for photocatalyst S-2.

3.3. Photocatalytic mechanism

It is generally known that a larger surface area of catalyst would be beneficial to the catalytic reaction through providing more active reaction sites. Hereby, the BET surface areas of the as-prepared samples (S-1, S-2, S-4, S-6, pure $BiPO_4$, pure Bi_2SiO_5) were investigated by N_2 adsorption and desorption isotherms, as shown in Figs. 5 and S3, and were found to be 0.5769, 19.5756, 49.4816, 60.7026, 4.9527 and 16.5485 $m^2 \cdot g^{-1}$, respectively. The results show that the BET specific surface areas of the as-prepared samples increased constantly as increasing the adding amount of SiO_3^{2-}. Compared with pure $BiPO_4$ and Bi_2SiO_5, when the adding amount of SiO_3^{2-} exceeds 1 mmol, the as-prepared samples (S-2, S-4 and S-6) all exhibit higher values of the BET specific surface area.

The UV–vis diffuse reflection spectra (DRS) of the as-prepared

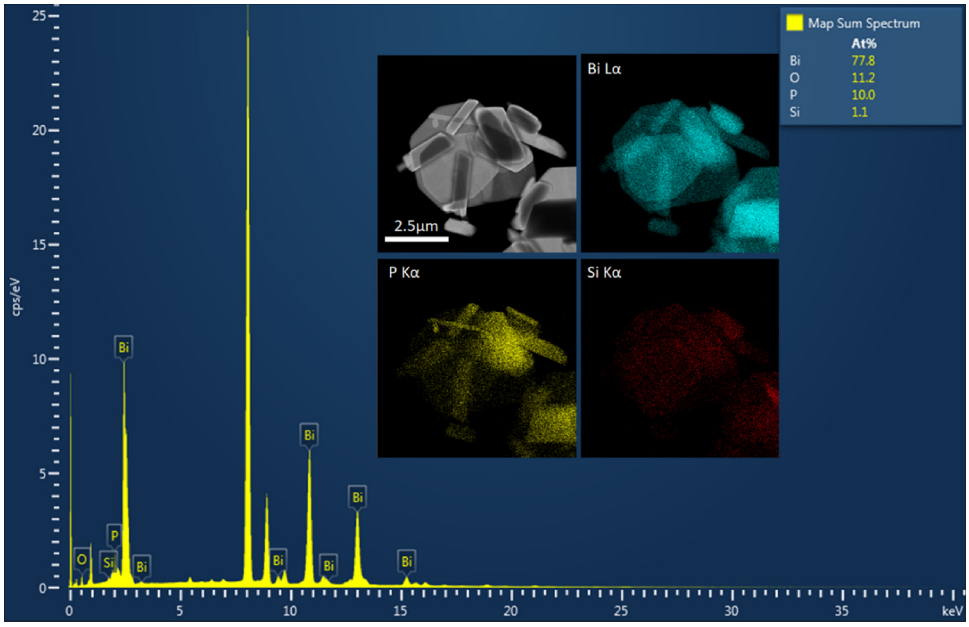

Fig. 3. EDX analysis of sample S-2 and the corresponding TEM image and elemental mapping of Bi, P, Si (inset).

samples are adopted to investigate their optical adsorption properties, as displayed in Fig. 8a. The absorption edge of pure $BiPO_4$ is estimated to be around 290 nm, implying its large band-gap. For the pure Bi_2SiO_5, its adsorption edge is located around 360 nm. Obvious red shifts were observed for the as-prepared heterostructured samples compared with pure $BiPO_4$ and Bi_2SiO_5, and slight absorption in the region of 370–500 nm increased gradually with increasing adding amount of SiO_3^{2-}. The band gap of the $Bi_2SiO_5/BiPO_4$ heterostructures can be calculated through the formula: $\alpha h\nu = A(h\nu - E_g)^{n/2}$, where α, h, υ, A and E_g represents absorption coefficient, Planck constant, light frequency, a constant, and band gap energy, respectively [30,31]. In this formula, the n is decided by the type of optical transition of a semiconductor (n = 1 for direct transition and n = 4 for indirect transition). The n values of Bi_2SiO_5 [32] and $BiPO_4$ [3] were both reported to be 4. As a result, through calculation from the plot of $(\alpha h\nu)^{2/n}$ versus $(h\nu)$ shown in Fig. 8b, the E_g of sample S-2 was estimated to be 3.2 eV. Therefore, it can be concluded that light absorption has been greatly expanded through introduction of the narrower bad-gap component Bi_2SiO_5, compared with pure $BiPO_4$.

The photocurrent test is known as a useful tool to reflect the separation and transfer efficiency of the photo-generated carrier under irradiation. Hereby, photocurrent response test was conducted on pure

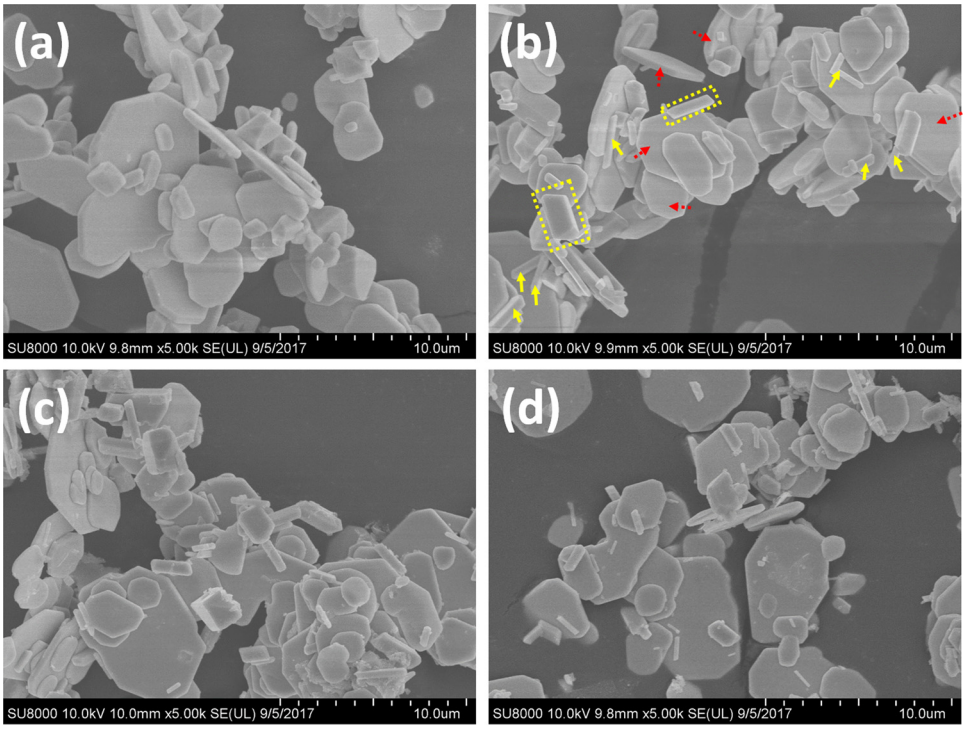

Fig. 4. SEM images of as-prepared samples at the magnification of 5.00K: S-1 (a), S-2 (b), S-4 (c) and S-6 (d). In Fig. 4b, the areas labeled by the dashed rectangles and the pointing areas by the solid arrows refer to the $BiPO_4$ micro-rods, whereas the pointing areas by the dotted arrows refer to the Bi_2SiO_5 plates.

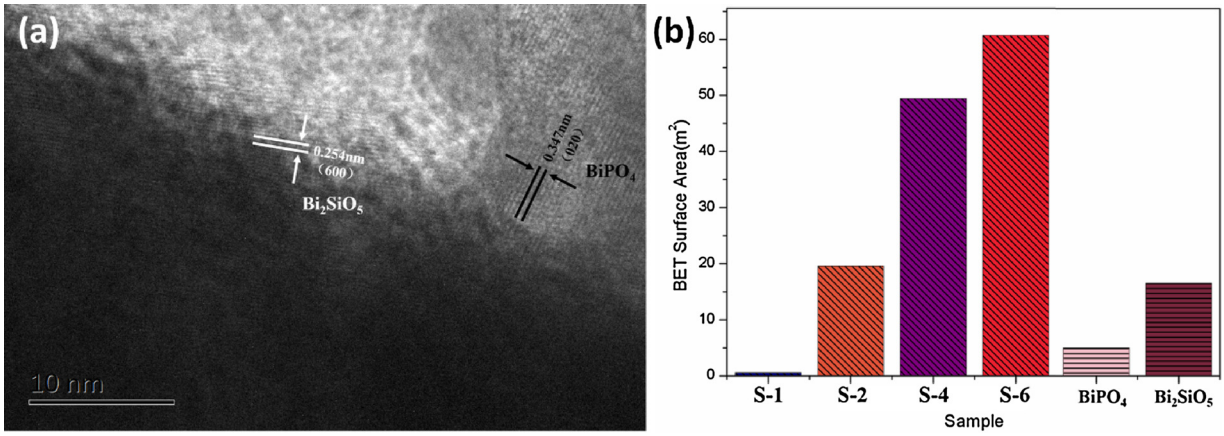

Fig. 5. HRTEM image of sample S-2 (a); BET surface areas of the as-prepared samples (b).

$BiPO_4$, pure Bi_2SiO_5 and sample S-2 under several 30 s on-off cycles under UV light irradiation. As can be seen in Fig. 9, pure $BiPO_4$ exhibits almost no photocurrent response due to its wide band gap, while $Bi_2SiO_5/BiPO_4$ heterostructure shows higher photocurrent response intensity than that of pure Bi_2SiO_5 and $BiPO_4$. Such an enhanced photocurrent response of $Bi_2SiO_5/BiPO_4$ heterostructure indicates an improvement in the separation and transfer efficiency of the photo-generated h^+/e^- pairs, which is in accordance with the photocatalytic performance shown above. EIS is also a powerful electrochemical technique to determine the kinetics of charge transfer in the composite electrode system. Fig. S4 shows the Nyquist plots of S-2 and Bi_2SiO_5, in which the arcs are related to the efficiency of charge transfer upon the interface of photo-electrode. Herein, obvious decreased diameters of arcs of S-2 compared with Bi_2SiO_5, indicated a smaller charge transfer resistance across the photoelectrode–liquid junction. Namely, the EIS spectra results revealed that the $Bi_2SiO_5/BiPO_4$ heterostructure of S-2 possess a higher charge carriers transfer efficiency compared with Bi_2SiO_5.

Based on the above results, a photocatalytic mechanism of the $Bi_2SiO_5/BiPO_4$ heterostructure under UV light irradiation is illustrated in Fig. 10, where the grey plate structure and dark blue rod structure correspond to Bi_2SiO_5 and $BiPO_4$, respectively. As shown in Fig. 10, the conduction band (CB) and valence band (VB) potentials of Bi_2SiO_5 were located at 0.05 and + 3.59 eV [22], respectively, while the CB and VB edge potentials of $BiPO_4$ were determined at -0.65 and + 3.20 eV [3], respectively. When the heterojunction was irradiated under UV light, e^- are excited from the valence band (VB) of Bi_2SiO_5 to the conduction band (CB) and created h^+ in the VB. The difference of chemical potential between $BiPO_4$ and Bi_2SiO_5 would drive the migration of photo-generated holes from the VB of Bi_2SiO_5 to VB of $BiPO_4$, which means $BiPO_4$ here can serve as a hole acceptor. Importantly, P in the PO_4^{3-} exhibits the highest valence state, thus it is hard to be oxidized by the holes which means the absence of anodic photo-corrosion. In such a way, a spatial separated photo-generated electrons and holes can be obtained upon their contact interface, leading to an enhanced charge separation efficiency. Considering the factors influencing the photocatalytic activity of a catalyst, such as crystal phase and crystallinity, morphology and size, BET specific surface area, electronic band structure and so forth, here the superior photocatalytic performance of sample S-2 under UV (365 nm) light irradiation can be attributed to (1) good crystallinity (less bulk defects) which means less carrier trap centers where e^--h^+ recombine, (2) the extended range of spectral response due to the existence of a narrower band-gap component Bi_2SiO_5 phase, (3) a moderate BET surface area which provides active reaction sites for the photocatalytic system, (4) the improved charge separation efficiency at the interface of the $Bi_2SiO_5/BiPO_4$ heterojunction owe to their well-aligned straddling band-structures.

4. Conclusion

We successfully constructed a novel type II heterostructure of $Bi_2SiO_5/BiPO_4$ through a simple co-precipitation method. Importantly, it not only exhibits a narrowed band gap due to the introduction of component of Bi_2SiO_5, but also shows highly enhanced photocatalytic activity compared with pure $BiPO_4$ and Bi_2SiO_5 under UV light (365 nm) irradiation. In addition, two components in $Bi_2SiO_5/BiPO_4$

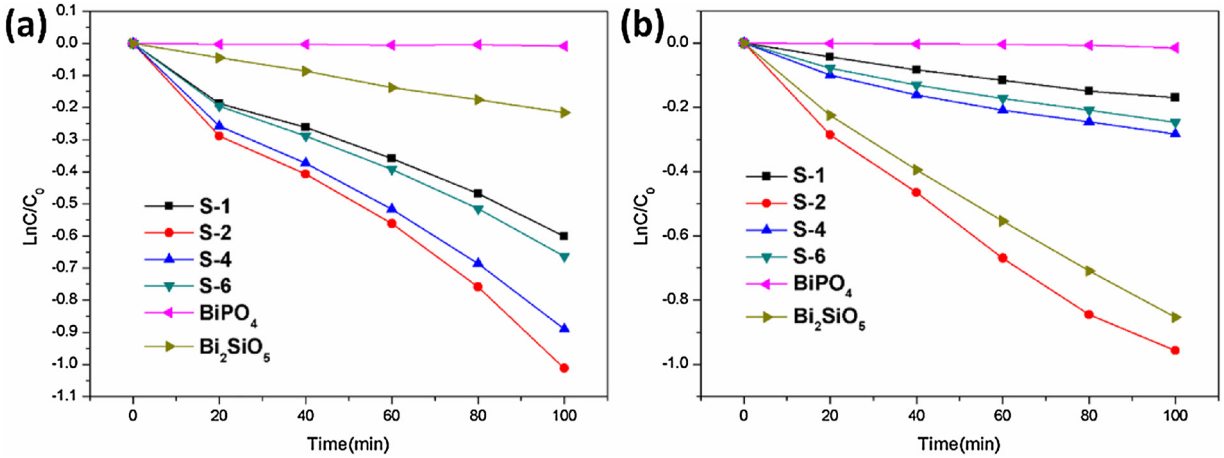

Fig. 6. Photocatalytic degradation efficiencies on phenol (a) and MB (b) by the as-prepared samples under UV-light (365 nm) irradiation.

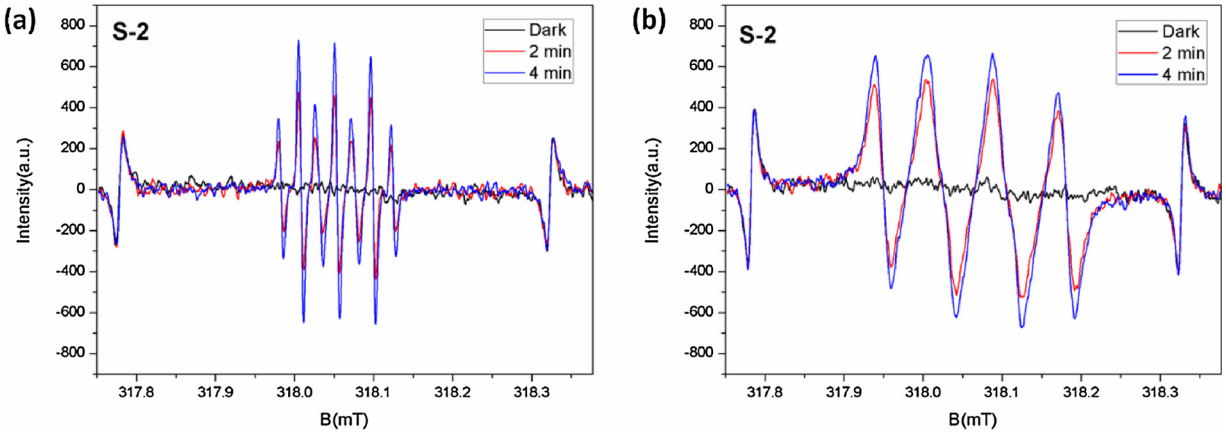

Fig. 7. ESR spectra upon UV light irradiation of S-2 suspension for detection of ·OH (a) and $O_2^{\cdot -}$ (b).

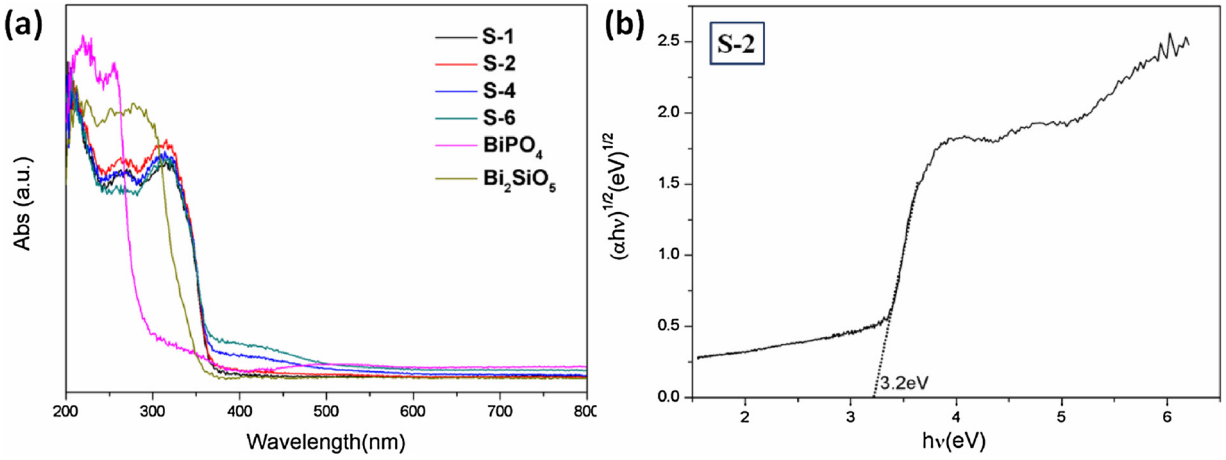

Fig. 8. UV–vis diffuse reflectance spectra of the as-prepared samples (a), the plot of $(ahυ)^{1/2}$ vs. hυ of sample S-2 (b).

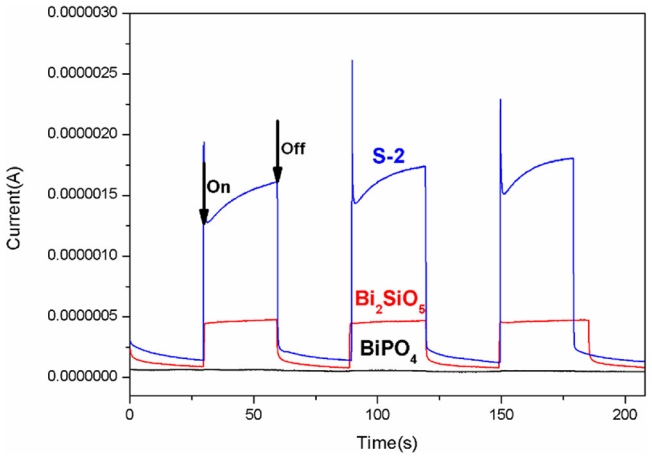

Fig. 9. The photocurrent of the as-prepared samples electrodes under UV-light (λ = 350 ± 10 nm) irradiation.

heterostructure with differentiable characteristics in the morphologies were revealed, Bi_2SiO_5 exhibits plates-like structure and $BiPO_4$ shows rods-like structure. It is found that the good crystallinity, efficient separation of photo-generated carriers via the $Bi_2SiO_5/BiPO_4$ heterostructure together with a moderate BET surface area would mainly contribute to its highly enhanced photocatalytic performance.

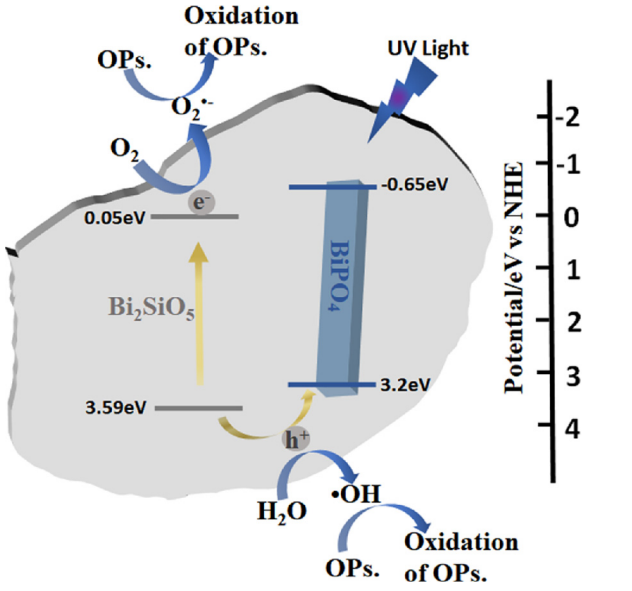

Fig. 10. Schematic illustration of the band-gap structure and possible flow of charge carriers in the Bi_2SiO_5 plates/$BiPO_4$ micro-rods heterostructure system under UV light (365 nm) irradiation.

Acknowledgement

This work was financially supported by China Postdoctoral Science Foundation (No. 2017M620073).

Appendix A. Supplementary data

Supplementary material related to this article can be found, in the online version, at doi: https://doi.org/10.1016/j.apcatb.2018.05.022.

References

[1] C. Pan, J. Xu, Y. Chen, Y. Zhu, Influence of OH-related defects on the performances of BiPO4 photocatalyst for the degradation of rhodamine B, Appl. Catal. B Environ. 115-116 (2012) 314–319.
[2] B.P. Nelson, R. Candal, R.M. Corn, M.A. Anderson, Control of surface and ζ potentials on nanoporous TiO2 films by potential-determining and specifically adsorbed ions, Langmuir 16 (2000) 6094–6101.
[3] C. Pan, Y. Zhu, New type of BiPO4 Oxy-acid Salt photocatalyst with High photocatalytic activity on degradation of dye, Environ. Sci. Technol. 44 (2010) 5570–5574.
[4] C. Pan, Y. Zhu, Size-controlled synthesis of BiPO4 nanocrystals for enhanced photocatalytic performance, J. Mater. Chem. 21 (2011) 4235–4241.
[5] H. Lin, H. Ye, B. Xu, J. Cao, S. Chen, Ag3PO4 quantum dot sensitized BiPO4: a novel p–n junction Ag3PO4/BiPO4 with enhanced visible-light photocatalytic activity, Catal. Commun. 37 (2013) 55–59.
[6] D. Wang, L. Yue, L. Guo, F. Fu, X. He, H. Shen, AgBr nanoparticles decorated BiPO4 microrod: a novel p-n heterojunction with enhanced photocatalytic activities, RSC Adv. 5 (2015) 72830–72840.
[7] H. Xu, Y. Xu, H. Li, J. Xia, J. Xiong, S. Yin, C. Huang, H. Wan, Synthesis, characterization and photocatalytic property of AgBr/BiPO4 heterojunction photocatalyst, Dalton Trans. 41 (2012) 3387–3394.
[8] H. Ye, H. Lin, J. Cao, S. Chen, Y. Chen, Enhanced visible light photocatalytic activity and mechanism of BiPO4 nanorods modified with AgI nanoparticles, J. Mol. Catal. A Chem. 397 (2015) 85–92.
[9] F. Duo, Y. Wang, X. Mao, X. Zhang, Y. Wang, C. Fan, A BiPO4/BiOCl heterojunction photocatalyst with enhanced electron-hole separation and excellent photocatalytic performance, Appl. Surf. Sci. 340 (2015) 35–42.
[10] W. An, W. Cui, Y. Liang, J. Hu, L. Liu, Surface decoration of BiPO4 with BiOBr nanoflakes to build heterostructure photocatalysts with enhanced photocatalytic activity, Appl. Surf. Sci. 351 (2015) 1131–1139.
[11] Z. Wu, J. Liu, Q. Tian, W. Wu, Efficient visible light formaldehyde oxidation with 2D p-n heterostructure of BiOBr/BiPO4 nanosheets at room temperature, ACS Sustain.e Chem. Eng. 5 (2017) 5008–5017.
[12] H. Dong, Z. Cao, R. Shao, Y. Xiao, W. He, Y. Gao, J. Liu, Enhancing visible light photocatalytic activity of BiOBr/rod-like BiPO4 through a heterojunction by a two-step method, RSC Adv. 5 (2015) 63930–63935.
[13] X. Jia, J. Cao, H. Lin, M. Zhang, X. Guo, S. Chen, Novel I-BiOBr/BiPO4 heterostructure: synergetic effects of I- ion doping and the electron trapping role of wide-band-gap BiPO4 nanorods, RSC Adv. 6 (2016) 55755–55763.
[14] Y. Liu, W. Yao, D. Liu, R. Zong, M. Zhang, X. Ma, Y. Zhu, Enhancement of visible light mineralization ability and photocatalytic activity of BiPO4/BiOI, Appl. Catal. B Environ. 163 (2015) 547–553.
[15] Y. Liu, P. Zhang, H. Lv, J. Guang, S. Li, J. Jiang, A nanosheet-like BiPO4/Bi2O2CO3 heterostructured photocatalyst with enhanced photocatalytic activity, RSC Adv. 5 (2015) 83764–83772.
[16] C. Pan, J. Xu, Y. Wang, D. Li, Y. Zhu, Dramatic activity of C3N4/BiPO4 photocatalyst with Core/Shell structure formed by self-assembly, Adv. Funct. Mater. 22 (2012) 1518–1524.
[17] Z. Li, B. Li, S. Peng, D. Li, S. Yang, Y. Fang, Novel visible light-induced g-C3N4 quantum dot/BiPO4 nanocrystal composite photocatalysts for efficient degradation of methyl orange, RSC Adv. 4 (2014) 35144–35148.
[18] J. Yuan, Q. Gao, X. Li, Y. Liu, Y. Fang, S. Yang, F. Peng, X. Zhou, Novel 3-D nanoporous graphitic-C3N4 nanosheets with heterostructured modification for efficient visible-light photocatalytic hydrogen production, RSC Adv. 4 (2014) 52332–52337.
[19] H. Lin, H. Ye, S. Chen, Y. Chen, One-pot hydrothermal synthesis of BiPO4/BiVO4 with enhanced visible-light photocatalytic activities for methylene blue degradation, RSC Adv. 4 (2014) 10968–10974.
[20] J. Li, H. Yuan, Z. Zhu, Fabrication of Cu2O/Au/BiPO4 Z-scheme photocatalyst to improve the photocatalytic activity under solar light, J. Mol. Catal. A Chem. 410 (2015) 133–139.
[21] R. Chen, J. Bi, L. Wu, W. Wang, Z. Li, X. Fu, Template-Free hydrothermal synthesis and photocatalytic performances of novel Bi2SiO5 nanosheets, Inorg. Chem. 48 (2009) 9072–9076.
[22] Z. Wan, G. Zhang, Synthesis and facet-dependent enhanced photocatalytic activity of Bi2SiO5/AgI nanoplate photocatalysts, J. Mater. Chem. A 3 (2015) 16737–16745.
[23] X. Zhou, J. Wu, Q. Li, T. Zeng, Z. Ji, P. He, W. Pan, X. Qi, C. Wang, P. Liang, Carbon decorated In2O3/TiO2 heterostructures with enhanced visiblelight-driven photocatalytic activity, J. Catal. 355 (2017) 26–39.
[24] Y. Liu, Y. Zhu, J. Xu, X. Bai, R. Zong, Y. Zhu, Degradation and mineralization mechanism of phenol by BiPO4 photocatalysis assisted with H2O2, Appl. Catal. B Environ. 142-143 (2013) 561–567.
[25] X. Liu, W. Wang, Y. Liu, B. Huang, Y. Dai, X. Qin, X. Zhang, In situ synthesis of Bi2S3/Bi2SiO5 heterojunction photocatalysts with enhanced visible light photocatalytic activity, RSC Adv. 5 (2015) 55957–55963.
[26] Y. Zhang, B. Shen, H. Huang, Y. He, B. Fei, F. Lv, BiPO4/reduced graphene oxide composites photocatalyst with high photocatalytic activity, Appl. Surf. Sci. 319 (2014) 272–277.
[27] D. Liu, W. Yao, J. Wang, Y. Liu, M. Zhang, Y. Zhu, Enhanced visible light photocatalytic performance of a novel heterostructured Bi4O5Br2/Bi24O31Br10/Bi2SiO5 photocatalyst, Appl. Catal. B Environ. 172-173 (2015) 100–107.
[28] L. Huang, X. Hu, S. Yuan, H. Li, T. Yan, L. Shi, D. Zhang, Photocatalytic preparation of nanostructured MnO2-(Co3O4)/TiO2 hybrids: the formation mechanism and catalytic application in SCR deNOx reaction, Appl. Catal. B Environ. 203 (2017) 778–788.
[29] J. Sun, X. Li, Q. Zhao, M. Tade´, S. Liu, Quantum-sized BiVO4 modified TiO2 microflower composite heterostructures: efficient production of hydroxyl radicals towards visible light-driven degradation of gaseous toluene, J. Mater. Chem. A 3 (2015) 21655–21663.
[30] J. Sun, X. Li, Q. Zhao, J. Ke, D. Zhang, Novel V2O5/BiVO4/TiO2 nanocomposites with High Visible-light induced photocatalytic activity for the degradation of toluene, J. Phys. Chem. C 118 (2014) 10113–10121.
[31] F. Zhang, X. Li, Q. Zhao, Q. Zhang, M. Tade´, S. Liu, Fabrication of a-Fe2O3/In2O3 composite hollow microspheres: a novel hybrid photocatalyst for toluene degradation under visible light, J. Colloid Interface Sci. 457 (2015) 18–26.
[32] C. Chen, C. Yang, W. Chung, J. Chang, W. Lin, Synthesis and characterization of Bi4Si3O12, Bi2SiO5, and Bi12SiO20 by controlled hydrothermal method and their photocatalytic activity, J. Taiwan Inst. Chem. Eng. 78 (2017) 157–167.